Research Article Vol. 33, No. 19 / 22 Sep 2025 / Optics Express 40931
Optics EXPRESS

Propagation of optical vector and scalar vortices in an atomic medium with closed-loop tripod configuration

VIAČESLAV KUDRIAŠOV,[1] MAZENA MACKOIT SINKEVIČIENĖ,[1] NILAMONI DALOI,[2] JULIUS RUSECKAS,[3] TARAK N. DEY,[4] SONJA FRANKE-ARNOLD,[5,*] AND HAMID R. HAMEDI[1]

[1]*Institute of Theoretical Physics and Astronomy, Vilnius University, Saulėtekio 3, Vilnius LT-10257, Lithuania*
[2]*School of Physics and Astronomy, Rochester Institute of Technology, Rochester, New York 14623, USA*
[3]*Baltic Institute of Advanced Technology, LT-01403 Vilnius, Lithuania*
[4]*Department of Physics, Indian Institute of Technology Guwahati, Guwahati 781039, Assam, India*
[5]*School of Physics and Astronomy, University of Glasgow, Glasgow G12 8QQ, United Kingdom*
[*]*Sonja.Franke-Arnold@glasgow.ac.uk*

Abstract: We investigate the propagation of an optical vector vortex beam in an atomic medium featuring four-level tripod transitions, where ground-state coherence is mediated by a transverse magnetic field. The vector beam consists of left- and right-circularly polarized components, each carrying an optical vortex with opposite orbital angular momentum (OAM). We study the linear response of the medium to the vector beam in order to determine the evolution of the beam's intensity and polarization profile. We find that the beam structure undergoes significant transformations as it propagates: the transverse intensity evolves from a ring-shaped profile to a petal-like structure, while the polarization transitions between left-circular, linear, and right-circular polarizations. Furthermore, when only the right-circular polarization component (a scalar vortex) enters the medium, it parametrically generates a left-circular polarization component, transferring its OAM to the generated field. This process converts the initial vortex beam into a superposition of left- and right-circular components, forming a scalar vortex beam where both polarization components carry the same OAM.

1. Introduction

Light beams carrying orbital angular momentum (OAM) [1] have become a key area of research in modern optics due to their unique phase structure and potential applications in areas such as optical communication and quantum information processing [2,3]. Unlike conventional Gaussian beams, which have a uniform phase front, OAM beams possess a helical phase structure of the form $e^{il\phi}$ where l is the topological charge corresponding to the amount of OAM per photon. The ability to encode information in this additional degree of freedom has led to significant interest in their generation, propagation, and interaction in various optical and quantum systems. These beams are notable for their ability to carry angular momentum, manipulate light in distinctive ways, and enable high-dimensional encoding, making them useful in advanced optical applications [4].

In atomic media, the propagation and evolution of optical fields are strongly influenced by quantum coherence and interference effects. These effects, arising from the coherent superposition of atomic states, give rise to a range of phenomena such as electromagnetically induced transparency (EIT) [5,6], slow light [7–9], and enhanced nonlinear interactions [10–12].

#566363 https://doi.org/10.1364/OE.566363
Journal © 2025 Received 28 Apr 2025; revised 21 Jul 2025; accepted 14 Aug 2025; published 18 Sep 2025

Optics EXPRESS

EIT, for instance, enables the transmission of light through an otherwise opaque medium by using a control field to create a transparency window. Quantum coherence effects in EIT alter the susceptibility of the medium, providing transparency or absorption windows for light [13,14]. The susceptibility of atom-light couplings can be affected by several factors, including the properties of light and the medium itself. Additionally, magnetic fields can influence atomic susceptibility by modifying the detuning and relaxation rates between energy levels [15,16]. A well-known phenomenon that exploits quantum interference between transition channels under magnetic fields is Hanle EIT, which uses magnetic field variation to split the Zeeman sublevels, resulting in a Lorentz-type transmission spectrum [17].

Given the distinctive features of both EIT-enabled atomic systems and optical vortex beams, their interaction has garnered considerable interest, leading to several intriguing phenomena. These include entanglement of OAM in four-wave mixing [18–20], OAM states of photon pairs [21], the transfer of OAM of slow light [22–24], and azimuthally dependent optical transparency governed by the phase of optical vortices [25]. However, the aforementioned studies predominantly focused on uniformly polarized (scalar) light fields, extracting information solely from the beam's overall transmission spectrum. In contrast, optical information can also be encoded in the polarization degree of freedom, which is parameterized by the optical spin [26]. Vector beams unify both the polarization and spatial information paradigms. Composed of orthogonal polarization components with different complex amplitudes, they exhibit spatially varying polarization profiles, thus offering a wide range of applications [27,28].

Optical vector vortex beams [29,30], owing to their spatially varying polarization distribution, offer a higher capacity for encoding and manipulating information [31,32]. Such beams can be generated by the vector superposition of two orthogonally polarized, OAM carrying Laguerre-Gaussian (LG) modes [33]. This results in a heterogeneous distribution of polarization on the transverse plane creating polarization vortices. The polarization distribution can be radially symmetric exhibiting radial, spiral, and azimuthal patterns when the two constituent LG modes have equal and opposite OAMs [27,34].

The interaction of polarization vortices with specific atomic structures can induce unique effects in atomic media [34–51]. Specifically, it has been experimentally shown that an optical vector vortex beam induces a spatially structured EIT effect in a four-level tripod atomic system [35], supported by a theoretical description via the dressed state picture. The full theoretical model was later presented in [52]. In this system, a weak transverse magnetic field closes the EIT transitions, generating phase-dependent dark states that result in phase-dependent transparency. This model was subsequently used to measure the strength and 3D spatial alignment of magnetic fields [39], as well as the optical concurrence of vector beams [37]. The interaction of vector light beams with atoms exposed to a time-dependent magnetic field has been explored more recently [42]. Additionally, a theoretical study [36] based on the density matrix formalism provided a deeper understanding of the phenomenon observed in [35].

In this paper, we investigate the azimuthally dependent phase and polarization evolutions in the four-level tripod atomic setup explored earlier [35,37,39]. Compared to the previous studies, which have primarily considered steady-state solutions focused on atomic coherence, here we present the full propagation dynamics of an optical vector vortex beam as it interacts with the atomic medium. By analytically solving the Maxwell-Bloch equations in the linear regime while neglecting transverse diffraction effects, we capture how both the intensity profile and the polarization state evolve during the propagation of vector beam. This propagation dynamics approach not only complements earlier steady-state coherence analyses, but also provides deeper insight into the mechanisms of beam reshaping and polarization transformation induced by atom-light interaction during light propagation. In particular, we demonstrate the exchange of OAM between light and atoms, showing how an initial vortex beam transfers its vorticity to a generated orthogonal polarization component. Understanding the full propagation dynamics of

Optics EXPRESS

beams carrying vortices is crucial for applications requiring precise control over OAM transfer between polarization components, such as vortex beam conversion in quantum systems, or for devices that exploit distance-dependent polarization structuring, like compact atomic sensors. Unlike steady-state models [35,37,39], our spatially resolved approach quantifies how beam transformations (in intensity and polarization) evolve with propagation length, providing a more comprehensive understanding that is essential for optimizing system design, medium thickness, and performance in applications where spatially varying effects are significant. The key novel aspects of this study — the spatial polarization conversion driven by the medium's anisotropic response and the OAM transfer between orthogonal circular polarization components — are discussed in detail in Sections 3.2 and 3.3, respectively. Although our analysis is restricted to the linear regime, it is advantageous in enabling straightforward analytical results, deepening physical insight and providing practical guidance.

2. Theoretical model

2.1. Atom-light configuration and energy diagram

We consider a four-level tripod system as shown in Fig. 1, interacting with a weak probe vector vortex beam $\vec{E} = E_L\hat{e}_L + E_R\hat{e}_R$ propagating along the $\hat{z}$-axis. Here, E_R and E_L are the slowly varying envelope functions for the right ($\hat{e}_R$) and left ($\hat{e}_L$) polarization components of the probe beam. We work in the weak probe regime, with light intensity well below saturation. The right-hand polarization component couples the transition $|1\rangle \leftrightarrow |4\rangle$ with Rabi frequency $\Omega_R = \vec{d}_R \cdot \hat{e}_R E_R/\hbar$, while the left-hand component couples $|3\rangle \leftrightarrow |4\rangle$ with $\Omega_L = \vec{d}_L \cdot \hat{e}_L E_L/\hbar$. All fields in the system co-propagate along the $\hat{z}$-axis. The atomic configuration can be realized, for example, for the D_2 transition ($5^2S_{1/2} \rightarrow 5^2P_{3/2}$) of a Rubidium (Rb) vapor, denoting the Zeeman sublevels of the $F = 1$ ground state as $|1\rangle = |5^2S_{1/2}, F = 1, m_F = -1\rangle$, $|2\rangle = |5^2S_{1/2}, F = 1, m_F = 0\rangle$, $|3\rangle = |5^2S_{1/2}, F = 1, m_F = +1\rangle$, and the $F' = 0$ excited state as $|4\rangle = |5^2P_{3/2}, F = 0, m_F = 0\rangle$. While the ground states $|1\rangle$, $|2\rangle$ and $|3\rangle$ are quasi-degenerate, the excited state $|4\rangle$ is well separated in energy.

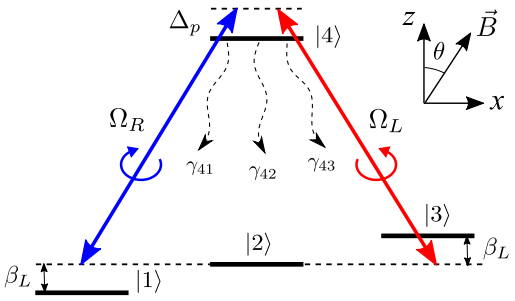

Fig. 1. Schematic diagram of a four-level closed atomic system. The transitions between states $|4\rangle \leftrightarrow |3\rangle$ and $|4\rangle \leftrightarrow |1\rangle$ are driven by circularly polarized components of the probe field, specifically left-handed ($\hat{e}_L$) and right-handed ($\hat{e}_R$) polarization, respectively. Zeeman sublevels $|1\rangle$, $|2\rangle$, and $|3\rangle$ interact through a weak transverse magnetic field $B\sin\theta$, where $\theta \ll \pi/2$. The radiative decay process from the excited state $|4\rangle$ to the ground states $|i\rangle$ ($i \in \{1, 2, 3\}$) is characterized by decay rates γ_{4i}. The probe beam propagates along the z-axis, which is also chosen as the quantization axis.

We consider an arbitrary magnetic field $\mathbf{B} = B(\cos\theta\hat{z} + \sin\theta\hat{x})$, where θ describes the polar angle between the magnetic field and the optical propagation axis $\hat{z}$, and $\hat{x}$ denotes the transverse direction of the field B. The longitudinal component $B_z = B\cos\theta$ introduces Zeeman shifts to ground levels $|1\rangle$ and $|3\rangle$, while the transverse component $B_x = B\sin\theta$ facilitates population

Optics EXPRESS

redistribution among ground states $|1\rangle$, $|2\rangle$ and $|3\rangle$. The angle θ, therefore, determines the balance between the energy level splitting and state mixing in the system. The transverse magnetic field component generates a closed-loop configuration, thereby inducing phase-dependent dark states which, in turn, lead to phase-dependent transparency [35]. In the absence of the transverse field, the atomic population predominantly accumulates in state $|2\rangle$. However, the introduction of a finite transverse component enables population redistribution among all three ground states, as will be analytically demonstrated in the next section. We introduce the parameters $\beta_L = \beta_0 \cos\theta$ and $\beta_T = \beta_0 \sin\theta/\sqrt{2}$ to quantify the Zeeman shift and magnetic ground state mixing, respectively. Here, $\beta_0 = g_F \mu_B B/\hbar$ where g_F denotes the Landé factor and μ_B is the Bohr magneton.

2.2. Optical Bloch equations for the light-atom interaction

Employing the electric dipole approximation and the rotating wave approximation (RWA), the Optical Bloch equations describing the system can be expressed as [36]

$$\dot{\rho}_{11} = \gamma_{41}\rho_{44} - i\beta_T\rho_{21} + i\beta_T\rho_{12} + i\Omega_R^*\rho_{41} - i\Omega_R\rho_{14} - 2\gamma_c\rho_{11} + \gamma_c\rho_{22} + \gamma_c\rho_{33}, \tag{1}$$

$$\dot{\rho}_{12} = i\beta_L\rho_{12} - i\beta_T(\rho_{22} - \rho_{11}) + i\beta_T\rho_{13} + i\Omega_R^*\rho_{42} - 2\gamma_c\rho_{12}, \tag{2}$$

$$\dot{\rho}_{13} = 2i\beta_L\rho_{13} - i\beta_T(\rho_{23} - \rho_{12}) + i\Omega_R^*\rho_{43} - i\Omega_L\rho_{14} - 2\gamma_c\rho_{13}, \tag{3}$$

$$\dot{\rho}_{14} = -i(\Delta_p - \beta_L)\rho_{14} - i\beta_T\rho_{24} + i\Omega_R^*(\rho_{44} - \rho_{11}) - i\Omega_L^*\rho_{13} - \Gamma_{41}\rho_{14}, \tag{4}$$

$$\dot{\rho}_{22} = \gamma_{42}\rho_{44} - i\beta_T(\rho_{12} - \rho_{21}) - i\beta_T(\rho_{32} - \rho_{23}) + \gamma_c\rho_{11} - 2\gamma_c\rho_{22} + \gamma_c\rho_{33}, \tag{5}$$

$$\dot{\rho}_{23} = i\beta_L\rho_{23} - i\beta_T\rho_{13} - i\beta_T(\rho_{33} - \rho_{22}) - i\Omega_L\rho_{24} - 2\gamma_c\rho_{23}, \tag{6}$$

$$\dot{\rho}_{24} = -i\Delta_p\rho_{24} - i\beta_T(\rho_{14} + \rho_{34}) - i\Omega_R^*\rho_{21} - \Gamma_{42}\rho_{24} - i\Omega_L^*\rho_{23}, \tag{7}$$

$$\dot{\rho}_{33} = \gamma_{43}\rho_{44} - i\beta_T(\rho_{23} - \rho_{32}) + i\Omega_L^*\rho_{43} - i\Omega_L\rho_{34} + \gamma_c\rho_{11} + \gamma_c\rho_{22} - 2\gamma_c\rho_{33}, \tag{8}$$

$$\dot{\rho}_{34} = -i(\Delta_p + \beta_L)\rho_{34} - i\beta_T\rho_{24} + i\Omega_L^*(\rho_{44} - \rho_{33}) - i\Omega_R^*\rho_{31} - \Gamma_{43}\rho_{34}. \tag{9}$$

The remaining density matrix equations are derived from the population conservation law $\sum_{i=1}^{4}\rho_{ii} = 1$ and the complex conjugate expressions $\dot{\rho}_{ji} = \dot{\rho}_{ij}^*$. The coherence decay terms $\Gamma_{4j}(j \in \{1,2,3\})$ are assumed to be equal $\Gamma_{41} = \Gamma_{42} = \Gamma_{43} = \Gamma$, and can be expressed as $\Gamma = \gamma_c + \frac{1}{2}\sum_{i=1}^{3}\gamma_{4i}$. We also assume that the excited state $|4\rangle$ decays to the ground states with equal rates, *i.e.*, $\gamma_{41} = \gamma_{42} = \gamma_{43} = \gamma/3$ where γ is the spontaneous decay rate of state $|4\rangle$. Furthermore, we consider the collision rate γ_c of the metastable ground states to be negligible, which is a reasonable assumption for cold atomic systems.

We now solve the density-matrix equations for the steady state. The probe field is assumed to be weak enough to be treated as a linear perturbation of the system. The perturbative expansion

Optics EXPRESS

of the density matrix up to first order in the probe field $\Omega_i (i \in \{R, L\})$ can be expressed as

$$\rho_{ij} = \rho_{ij}^{(0)} + \frac{\Omega_R}{\gamma}\rho_{ij}^{(1)} + \frac{\Omega_L}{\gamma}\rho_{ij}^{(1)}, \tag{10}$$

where $\rho_{ij}^{(0)}$ is the zeroth-order solution, which can be determined using the counterintuitive approach as [36]

$$\rho_{11}^{(0)} = \left(\frac{\beta_T}{\beta_L}\right)^2, \quad \rho_{22}^{(0)} = 1 - 2\left(\frac{\beta_T}{\beta_L}\right)^2, \tag{11}$$

and

$$\rho_{12}^{(0)} = \frac{\beta_L\beta_T\left(\rho_{22}^{(0)} - \rho_{11}^{(0)}\right)}{\beta_L^2 - \beta_T^2}, \tag{12}$$

$$\rho_{13}^{(0)} = -\frac{\beta_T^2\left(\rho_{22}^{(0)} - \rho_{11}^{(0)}\right)}{\beta_L^2 - \beta_T^2}, \tag{13}$$

$$\rho_{23}^{(0)} = -\frac{\beta_L\beta_T\left(\rho_{22}^{(0)} - \rho_{11}^{(0)}\right)}{\beta_L^2 - \beta_T^2}, \tag{14}$$

with all other matrix elements equal to 0. The second and third terms in Eq. (10) denote first-order solutions of the density matrix elements for both orthogonal polarizations at positive probe field frequency ω_p. Note that the solutions in Eqs. (11)–(14) are valid when $\beta_T \ll \beta_L$, or equivalently, $\theta \ll \pi/2$.

We now substitute Eq. (10) into Eqs. (1)–(9) and get the steady state solutions for the first-order density-matrix elements

$$\rho_{41}^{(1)} = \frac{N_1}{D}\Omega_R + \beta_T^2\frac{N_2}{D}\Omega_L, \tag{15}$$

$$\rho_{43}^{(1)} = \frac{N_3}{D}\Omega_L + \beta_T^2\frac{N_2}{D}\Omega_R, \tag{16}$$

with the coefficients defined as

$$N_1 = \gamma\beta_L^2 X\left(X + \beta_L\right)\rho_{11}^{(0)} + \gamma\beta_T^4\left(2\rho_{11}^{(0)} - \rho_{22}^{(0)}\right) - \gamma\beta_T^2\left[\rho_{11}^{(0)}X^2 + \beta_L\rho_{22}^{(0)}\left(X + \beta_L\right)\right], \tag{17}$$

$$N_2 = \gamma X^2\left(\rho_{11}^{(0)} - \rho_{22}^{(0)}\right) + \gamma\beta_L^2\rho_{22}^{(0)} - \gamma\beta_T^2\left(2\rho_{11}^{(0)} - \rho_{22}^{(0)}\right), \tag{18}$$

$$N_3 = \gamma\beta_L^2 X\left(X - \beta_L\right)\rho_{11}^{(0)} + \gamma\beta_T^4\left(2\rho_{11}^{(0)} - \rho_{22}^{(0)}\right) - \gamma\beta_T^2\left[\rho_{11}^{(0)}X^2 + \beta_L\rho_{22}^{(0)}\left(X - \beta_L\right)\right], \tag{19}$$

$$D = \left(\beta_L^2 - \beta_T^2\right)\left(\beta_L^2 + 2\beta_T^2 - X^2\right)X, \tag{20}$$

where $X = \Delta_p + i\Gamma$, with Δ_p and Γ representing the probe field detuning and the decay rate of the excited state, respectively.

Optics EXPRESS

2.3. Maxwell-Bloch equations for fields and their solution

To study the dynamics of light propagation in the medium, we begin by analyzing the Maxwell-Bloch (MB) equations for the probe fields. Neglecting the diffraction effects, MB equations for the optical Rabi frequencies Ω_R and Ω_L can be written as follows

$$\frac{\partial \Omega_R}{\partial z} = 2ik\chi_{41}\Omega_R, \tag{21}$$

$$\frac{\partial \Omega_L}{\partial z} = 2ik\chi_{43}\Omega_L, \tag{22}$$

where the corresponding linear optical susceptibilities are

$$\chi_{41} = \frac{N|d_R|^2}{\epsilon_0\hbar\gamma}\rho_{41}^{(1)}, \tag{23}$$

$$\chi_{43} = \frac{N|d_L|^2}{\epsilon_0\hbar\gamma}\rho_{43}^{(1)}. \tag{24}$$

Here N is the atomic density of the medium, and d_R, d_L denote the dipole moments of the corresponding probe transitions.

The diffraction terms containing the transverse derivatives $\nabla_\perp^2\Omega_R$ and $\nabla_\perp^2\Omega_L$ have been omitted in the Eqs. (21), (22). These terms are negligible if the phase change induced by diffraction remains much smaller than π. The diffraction effect can be estimated as $\nabla_\perp^2\Omega_{R(L)} \sim w^{-2}\Omega_{R(L)}$, where w represents the characteristic transverse dimension of the probe beams, either as the width of a vortex core (if present) or the typical beam width in the absence of a vortex. The temporal evolution of the probe fields is approximately $\partial\Omega_{R(L)}/\partial t \sim c\,\Omega_{R(L)}/L$, where L denotes the medium length. The resulting phase change due to diffraction is given by $L/(2kw^2)$, where k is the wave number of the probe fields. This contribution can be neglected when the condition $L\lambda/w^2 \ll 1$ holds, ensuring that diffraction effects are insignificant.

Using Eqs. (15), (16) and (23), (24), Eqs. (21), (22) can be transformed into a linear system of differential equations

$$\frac{\partial \Omega_R}{\partial z} = \frac{iFN_1}{D}\Omega_R + \frac{iFN_2\beta_T^2}{D}\Omega_L, \tag{25}$$

$$\frac{\partial \Omega_L}{\partial z} = \frac{iFN_2\beta_T^2}{D}\Omega_R + \frac{iFN_3}{D}\Omega_L, \tag{26}$$

where we define the coupling strength

$$F = \frac{2kN|d|^2}{\epsilon_0\hbar\gamma}, \tag{27}$$

and assume $|d_R| = |d_L| = |d|$.

Next, considering $\Omega_L(0)$ and $\Omega_R(0)$ as the field values at the medium's entrance, the general solutions for system (25–26) can be found (for the case $\beta_T \neq 0$) as

$$\Omega_R(z) = a\,\Omega_R(0) + c\,\Omega_L(0), \tag{28}$$

$$\Omega_L(z) = c\,\Omega_R(0) + b\,\Omega_L(0). \tag{29}$$

where we introduced coefficients

$$a = \frac{1}{2}\left[(e^{m_1 z} + e^{m_2 z}) + \frac{N_1 - N_3}{M}\,(e^{m_1 z} - e^{m_2 z})\right], \tag{30}$$

Optics EXPRESS

$$b = \frac{1}{2}\left[(e^{m_1 z} + e^{m_2 z}) - \frac{N_1 - N_3}{M}(e^{m_1 z} - e^{m_2 z})\right], \tag{31}$$

$$c = \frac{N_2 \beta_T^2}{M}(e^{m_1 z} - e^{m_2 z}), \tag{32}$$

and notations

$$m_{1,2} = \frac{iF}{2D}(N_1 + N_3 \pm M), \tag{33}$$

$$M = \sqrt{(N_1 - N_3)^2 + 4N_2^2\beta_T^4}. \tag{34}$$

In Eq. (33) m_1, m_2 correspond to +, − sign, respectively. The propagation of the optical system is fully described by Eqs. (28)–(29) together with the definitions of the various parameters. In the following sections we will analyze the propagation distance over which these equations hold and illustrate their implication for several cases of entrance fields $\Omega_L(0)$ and $\Omega_R(0)$.

3. Results and analysis

Analytical solutions for the field propagation, given by Eqs. (28)–(29), enable the study of the evolution of the Ω_L and Ω_R beams within the medium. In what follows, we first examine the characteristic propagation distances over which these solutions remain valid. Subsequently, we investigate the propagation dynamics of both vector and scalar vortex beams inside the medium.

3.1. Limits for the propagation distance

The expressions for m_1 and m_2 given in Eq. (33) are not purely imaginary; they depend on N_1, N_3, and M, which in turn depend on X, a complex number. Consequently, all exponents in the solutions provided in Eqs. (28) and (29) exhibit decay over large propagation distances z. As a result, the fields $\Omega_R(z)$ and $\Omega_L(z)$ should asymptotically approach zero for sufficiently large z, according to these equations. This implies that at very large z, state $|2\rangle$ becomes populated.

Beyond a certain propagation distance, the linear solutions (15) and (16) are no longer valid, necessitating the inclusion of nonlinear terms in calculating the density matrix elements ρ_{41} and ρ_{43}. However, these linear solutions remain valid for relatively short distances. To quantify this limitation, we define the characteristic propagation distance z_c, within which our solutions hold, but beyond which the linear regime breaks down due to strong absorption.

The exponential terms $e^{m_1 z}$ and $e^{m_2 z}$ in coefficients of Eqs. (28) and (29) can be rewritten as

$$e^{m_{1(2)} z} = e^{\mathrm{Re}(m_{1(2)})z} \cdot e^{i\mathrm{Im}(m_{1(2)})z}, \tag{35}$$

where the first factor represents exponential attenuation (for $\mathrm{Re}(m_{1,2})<0$), while the second term describes oscillatory behavior. The linear susceptibility model assumes weak absorption, which remains valid under the condition

$$|\mathrm{Re}(m_{1,2})| z \ll 1. \tag{36}$$

Beyond this regime, exponential decay dominates. The characteristic propagation distance z_c is approximately given by

$$z_c \approx \frac{1}{\max(|\mathrm{Re}(m_1)|, |\mathrm{Re}(m_2)|)}, \tag{37}$$

which ensures that neither exponential term decays significantly within the validity range of the linear approximation in Eq. (10). Thus, the linear susceptibility model holds for propagation distances $z<z_c$, where z_c is determined by the dominant decay rate among m_1 and m_2.

Since finding an analytical expression for $\mathrm{Re}(m_1)$ and $\mathrm{Re}(m_2)$ is highly complex due to their intricate dependence on N_1, N_3, M, D, and other system parameters, we resort to numerical calculations to determine the characteristic distance z_c. Fig. 2 illustrates the variation of the

Optics EXPRESS

characteristic distance z_c as a function of polar angle θ in the range $\pi/30 \leq \theta \leq \pi/14$. It is important to note that in the limit $\theta = 0$, the transverse component of the magnetic field vanishes, and the system reduces to a pure Zeeman configuration. In this case, the coupling strength between the ground states becomes zero ($\beta_T = 0$), causing the second terms in Eqs. (15) and (16) to vanish. This breaks the closed-loop configuration of the system, rendering it phase-insensitive, which is not the focus of this paper, where we are primarily interested in phase-sensitive features. On the other hand, Eq. (11) motivates operating in a regime where the transverse component of the magnetic field remains significantly weaker than the longitudinal component, *i.e.*, $\theta \ll \pi/2$. Additionally, Fig. 2 presents this variation under the resonance condition $\Delta_p = 0$. We observe from Fig. 2 that the characteristic distance z_c is largest for the smallest value of $\theta = \pi/30$, and it decreases as θ increases.

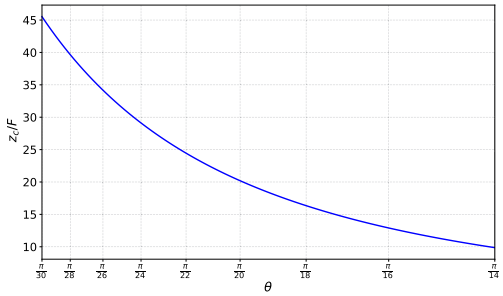

Fig. 2. Characteristic distance z_c versus magnetic field angle θ. The parameters used are $\beta_0 = 0.01\gamma$, $\Gamma_{41} = 0.5\gamma$, $\Delta_p = 0$.

Figure 3 shows the variation of the characteristic distance z_c versus probe detuning for $\theta = \pi/30$, where the characteristic distance reaches its maximum, as seen in Fig. 2. From Fig. 3, we observe that the characteristic distance is minimum at the resonance condition $\Delta_p = 0$ and increases as we move away from resonance. Based on the plots, for $\theta = \pi/30$, the characteristic distance at resonance ($\Delta_p = 0$) can be approximated as $z_c \sim 45/F$, while for the non-resonance case $\Delta_p = 2\gamma$, it can be estimated as $777/F$. The characteristic distance obtained from our analytical and numerical models, as shown in Figs. 2 and 3 will inform our evaluation of the propagation of the fields Ω_L and Ω_R in the following sections.

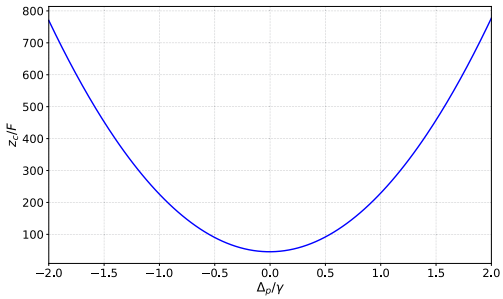

Fig. 3. Characteristic distance z_c versus probe detuning Δ_p. The parameters used are $\beta_0 = 0.01\gamma$, $\Gamma_{41} = 0.5\gamma$, $\theta = \pi/30$.

It may be worth estimating these propagation distances using realistic experimental parameters. According to Eq. (27), the coupling strength F depends on the atomic density N, the dipole moment magnitude $|d|$, and the decay rate γ, all of which are well-characterized for the ^{87}Rb D_2 transition. Using typical values for these parameters, such as $N = 2 \times 10^{11}$ cm^{-3},

Optics EXPRESS

$|d| \sim 2.54 \times 10^{-29}$ C · m, and $\gamma = 2\pi \times 6$ MHz, the coupling strength F can be calculated as $F \sim 5.91 \times 10^4$ m^{-1}. Once F is determined, any propagation distance can be easily calculated. For instance, for $\theta = \pi/30$ considered in this paper, the characteristic propagation distance z_c for the resonance condition ($\Delta_p = 0$) can be estimated as $z_c \sim 45/F \sim 0.00076$ m = 0.76 mm. For the non-resonant case ($\Delta_p = 2\gamma$) where we have determined $z_c \sim 777/F$, one can estimate its value to be $z_c \sim 0.0131$ m = 1.31 cm.

3.2. Propagation of vector vortex beams: structured atom-light interaction

Now, we assume that the fields Ω_R and Ω_L entering the medium are optical vortices having opposite OAM. Specifically, both fields are taken to be Laguerre-Gaussian (LG) modes of the lowest radial order, *i.e.*, LG_0^l. They can be expressed as:

$$\Omega_R(0) = |\Omega|\mathrm{LG}^R = A(r)e^{il\phi}, \tag{38}$$

$$\Omega_L(0) = |\Omega|\mathrm{LG}^L = A(r)e^{-il\phi}, \tag{39}$$

where $|\Omega|$ denotes the Rabi amplitude, and

$$A(r) = \left(\frac{r}{w}\right)^{|l|} e^{-\frac{r^2}{w^2}}, \tag{40}$$

represents the beam amplitude, with $\pm l$ denoting the OAM numbers and w denoting the beam radius. The resulting vortex beam at the entrance to the medium takes the form

$$\hat{E}(r, \phi, 0) = E_L(0)\hat{e}_L + E_R(0)\hat{e}_R = \cos(\alpha)\mathrm{LG}^L\hat{e}_L + e^{i\psi}\sin(\alpha)\mathrm{LG}^R\hat{e}_R, \tag{41}$$

where α defines relative amplitude, and ψ is the phase between the two LG modes at the entrance to the medium. These beams generally carry a net OAM which varies as a function of α. For the special case $\alpha = \pi/4$, *i.e.* $\cos(\alpha) = \sin(\alpha)$, the beam forms a vector vortex beam with spatially varying linear polarization and zero net OAM. By varying α, the resulting beam structure smoothly interpolates between purely circularly polarized vortex beams carrying OAM of $\pm l$, and the vector vortex beam at $\alpha = \pi/4$. We note that these beams have recently been used in [37] for measuring the optical concurrence of vector beams with an atomic-state interferometer.

Once the fields enter the medium, according to Eqs. (28–29) the beam components evolve with propagation distance z as

$$\Omega_R(z) = |\Omega|(a\,\mathrm{LG}^R + c\,\mathrm{LG}^L), \tag{42}$$

$$\Omega_L(z) = |\Omega|(c\,\mathrm{LG}^R + b\,\mathrm{LG}^L), \tag{43}$$

with a, b and c as previously defined in Eqs. (30)–(32).

It is evident that the combination of opposite LG modes at the entrance forms a more complex optical vector vortex beam, which continues to propagate through the medium. The corresponding electric field is given by $\hat{E}(r, \phi, z) = E_L\hat{e}_L + E_R\hat{e}_R$ where

$$E_L = \cos(\alpha)\left[c\,\mathrm{LG}^R + b\,\mathrm{LG}^L\right], \tag{44}$$

$$E_R = e^{i\psi}\sin(\alpha)\left[a\,\mathrm{LG}^R + c\,\mathrm{LG}^L\right], \tag{45}$$

represent the left and right circularly polarized field components of the vector beam, while $\{\hat{e}_L, \hat{e}_R\}$ represents the circular polarization basis. The resulting beam exhibits a correlation between its spin and OAM.

Optics EXPRESS

To illustrate the spatial dependence of polarization during beam propagation, we define the Stokes parameters in the circular polarization basis

$$S_0 = |E_R|^2 + |E_L|^2, S_1 = 2\mathrm{Re}(E_R^* E_L), S_2 = 2\mathrm{Im}(E_R^* E_L), S_3 = |E_R|^2 - |E_L|^2. \quad (46)$$

These parameters define ellipticity $\zeta = \frac{1}{2}\sin^{-1}(S_3/S_0)$ and orientation angle $\xi = \frac{1}{2}\tan^{-1}(S_2/S_1)$, which both characterize the polarization at each point in the medium [34]. After propagating a distance z through the medium, the polarization at each point on the vector beam's transverse plane rotates by an angle $\Delta\xi(z) = \xi(z) - \xi(0)$.

In what follows, we explore the intensity distribution and polarization of generated optical vector vortex beam featured in Eqs. (44)–(45) during its propagation inside the atomic cloud for the simplest example of singly charged vortex beams with $l = 1$ in Eqs. (38) and (39). We consider propagation distances z less than the characteristic distance z_c. The parameters are chosen to satisfy the characteristic distance limits given in Eq. 37 and depicted in Figs. 2 and 3. Fig. 4 corresponds to the resonance case $\Delta_p = 0$, while Fig. 5 represents the non-resonance condition $\Delta_p = 2\gamma$. In both cases, we set $\beta_0 = 0.01\gamma$ and $\theta = \pi/30$. In Fig. 4, the propagation distances are $Fz = 0, 15, 25$, and 40, satisfying $z<z_c \sim 45/F$ as determined in Fig. 2. Similarly, in Fig. 5, the propagation distances are $Fz = 0, 100, 300$ and 600, all within the limit $z<z_c \sim 777/F$. As seen in both figures, at $z = 0$ (*i.e.*, at the entrance of the atomic medium), the intensity profile of the vector beam at this stage is characterized by a doughnut shape, indicated by the dark ring. The polarization distribution of the vector beam exhibits uniform left-circular polarization (red ellipses) across all spatial patterns, with different polarization textures: radial (a), spiral (e), and azimuthal (i) for $\psi = 0, \pi/2$, and π, respectively. This occurs because the left-circular component in Eq. (41), E_L, dominates over the right-circular component E_R, due to the choice of relative amplitude $\alpha = \pi/8$, which results in $\cos(\alpha) > \sin(\alpha)$, leading to $|E_L| > |E_R|$. Note that the phase parameter ψ controls the spatial polarization texture (radial, spiral, or azimuthal), but does not affect the handedness, which depends solely on the amplitude ratio E_L/E_R.

As the beam propagates through the medium, significant modifications occur in both the intensity and polarization distributions. Notably, the intensity distribution no longer retains the ring-shaped profile, but instead transforms into a petal-like pattern, due to the superposition of the left- and right-handed LG beams, as described by Eqs. (44) and (45). This transformation is a direct consequence of interference between the helical phase structures of the LG modes ($\exp(\pm il\phi)$), which redistributes energy in the transverse plane. While the intensity profile of the vector vortex beam itself has a uniform azimuthal intensity (as the opposite orthogonal polarization components do not interfere), interaction with the atomic medium may be interpreted as an atomic state interferometer, where optical coupling together with coupling through the transverse magnetic field between $|1\rangle$, $|2\rangle$ and $|3\rangle$ facilitates interference. The azimuthally varying phase difference between E_L and E_R modulates the intensity, creating alternating maxima and minima that form the observed petals. The polarization evolution is governed by the coefficients a, b, and c, which evolve due to the medium's dispersive and absorptive response. These coefficients control the balance between E_L and E_R, thereby affecting the size, shape, and degree of entanglement of the polarization ellipses, making them wider or more entangled. Consequently, the radial, spiral, and azimuthal polarization patterns evolve as the beam propagates.

Under resonance condition (Fig. 4), the coefficients evolve monotonically, preserving the dominance of $E_L(|E_L| > |E_R|)$ throughout propagation. This maintains uniform left-circular polarization (red ellipses). The radial, spiral, or azimuthal polarization textures evolve spatially, but the beam retains its left-circular polarization throughout propagation. In contrast, in the non-resonance case (Fig. 5), the polarization state, which starts as left-handed at $z = 0$, oscillates during propagation. The non-resonant condition ($\Delta_p \neq 0$) introduces oscillatory dynamics via the complex eigenvalues m_1 and m_2, which modulate E_L and E_R through the coefficients a, b, and c. This results in periodic energy exchange between E_L and E_R and transforms the polarization

Optics EXPRESS

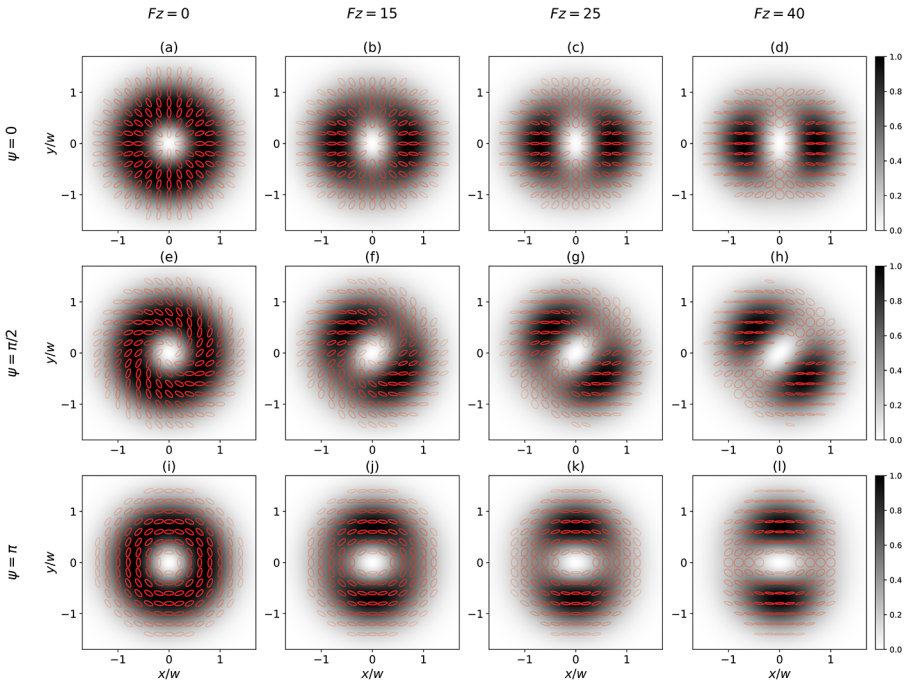

Fig. 4. Transverse intensity and polarization distributions as functions of x/w and y/w for a vector vortex beam with $|l| = 1$. The spatial coordinates are normalized to the beam waist w. The system is considered under the resonance condition $\Delta_p = 0$, with other parameters set to $\beta_0 = 0.01\gamma$, $\theta = \pi/30$, and $\alpha = \pi/8$. The first, second, and third rows show plots generated for $\psi = 0, \pi/2$, and π, respectively, while the first, second, third and fourth columns correspond to $Fz = 0, 15, 25$, and 40. These distances are chosen to be smaller than the characteristic distance z_c, as determined in Eq. (37) and illustrated in Fig. 2. The red colors of polarization correspond to left circular polarization.

state, alternating between left-handed (red ellipses), linear (yellow lines), and right-handed (blue ellipses) circular polarizations at different distances. At intermediate distances (*e.g.*, $Fz = 300$), the azimuthal phase structure of the LG modes introduces a position-dependent phase difference between E_L and E_R, leading to localized regions where all polarization states coexist. At larger propagation distances, close to the characteristic distance (*e.g.*, $Fz = 600$), the evolution of the system favors the dominance of E_R, resulting in a complete and uniform transition to right-handed circular polarization.

Figure 5 shows that, within the characteristic distance, there is a transition to a different polarization state during the propagation of the beam under non-resonance conditions, while the resonance condition shown in Fig. 4 lacks such a transition. The detuning Δ_p strongly influences the propagation distance at which this transition occurs. To visualize this polarization transformation more clearly, Fig. 6 presents a density plot showing the evolution of the spatially averaged polarization ellipticity angle ζ as a function of the detuning Δ_p/γ and the propagation distance Fz. It is evident from Fig. 6 that the propagation distance z, at which the polarization transition occurs strongly depends on the detuning. The results are in good agreement with those shown in Figs. 4 and 5. In particular, for the resonant case $\Delta_p = 0$, as seen in Fig. 6 the beam maintains its initial left-handed circular polarization (indicated by dark red) throughout propagation, but below the characteristic distance $z<z_c \sim 45/F$, with no observable transition — consistent with Fig. 4. On the other hand, for off-resonant cases ($\Delta_p \neq 0$), the transition distance

Optics EXPRESS

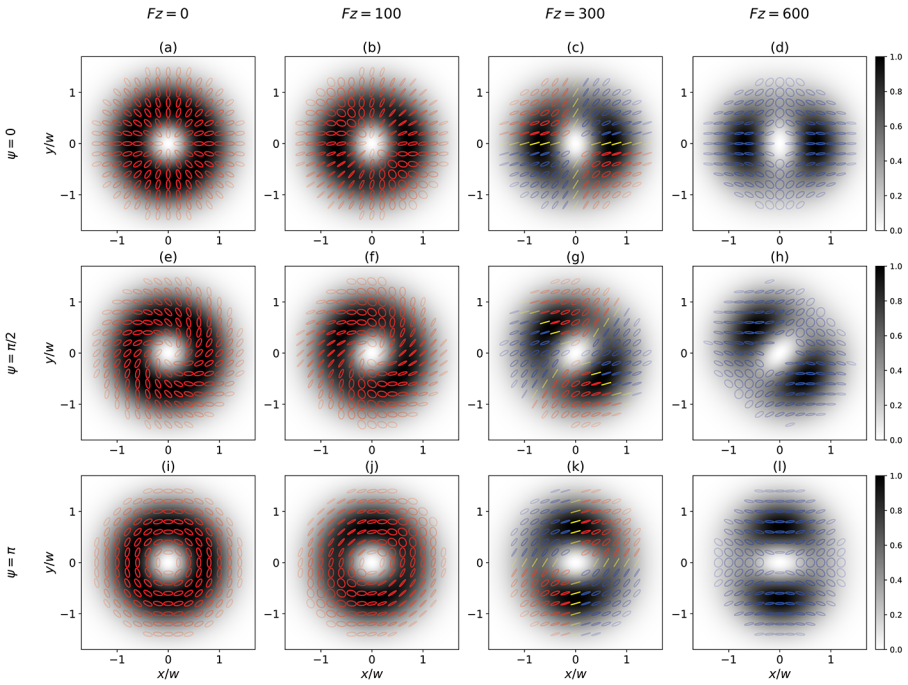

Fig. 5. Transverse intensity and polarization distributions as functions of x/w and y/w for a vector vortex beam with $|l| = 1$. The spatial coordinates are normalized to the beam waist w. The system is considered under the non-resonance condition $\Delta_p = 2\gamma$, with other parameters set to $\beta_0 = 0.01\gamma$, $\theta = \pi/30$, and $\alpha = \pi/8$. The first, second, and third rows show plots generated for $\psi = 0, \pi/2$, and π, respectively, while the first, second, third and fourth columns correspond to $Fz = 0, 100, 300$, and 600. These distances are chosen to be smaller than the characteristic distance z_c, as determined in Eq. (37) and illustrated in Fig. 3. The red, yellow and blue colors of polarization correspond to left-circular, linear, and right-circular polarizations, respectively.

increases with detuning, as also indicated in Fig. 5. In particular for $\Delta_p = 2\gamma$, Fig. 6 shows that different polarization states coexist at $Fz = 300$, including linear (white), left-handed circular (red), and right-handed circular (blue) polarizations. This observation agrees with Fig. 5(c, g, k). However, after further propagation (*e.g.*, at $Fz = 600$), the entire field evolves into a right-handed circular polarization state (blue), in agreement with Fig. 5(d, h, l). The use of white color to represent linear polarization in Fig. 6 provides clearer contrast compared to the yellow used for linear polarization in Fig. 5.

The observed polarization dynamics are a consequence of anisotropic response of the medium and arise from the interplay of magneto-optical effects, namely, circular birefringence (leading to a rotation of the polarization direction through the Faraday effect) and circular dichroism (which alters ellipticity). Circular dichroism, caused by differential absorption of right- and left-circular components, modifies the ellipticity and intensity of the beam. Which component is more strongly absorbed depends on the orientation of the polarization ellipse relative to the applied magnetic field (which lies along the x direction in our model). When the major axis of the ellipse is aligned with the field, the left-handed component is preferentially absorbed, making the light more linear; when perpendicular, the right-handed component is absorbed, making it more circular. The spatial variation of this effect across the beam depends on the local polarization geometry and is influenced by the Larmor frequency, which is small in our simulations. In the

Optics EXPRESS

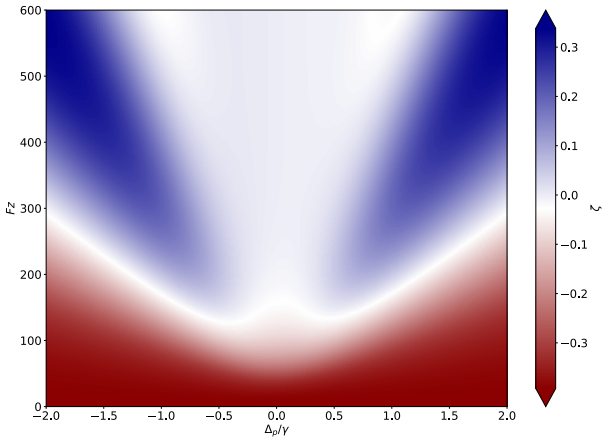

Fig. 6. Density plot showing the evolution of the spatially averaged polarization ellipticity angle ζ as a function of the detuning Δ_p/γ and the propagation distance Fz. The ellipticity angle is defined as $\zeta = \frac{1}{2}\sin^{-1}(S_3/S_0)$, where S_0 and S_3 are the Stokes parameters associated with the total intensity and the circular polarization component, respectively. The ellipticity is averaged over the transverse beam region where the intensity exceeds 10% of its peak value within r<1.5w. The colorbar indicates the polarization state: red corresponds to left-handed circular polarization, blue to right-handed circular polarization, and white to linear polarization.

off-resonant case (Fig. 5), one Zeeman-shifted absorption line dominates, enhancing differential absorption and even reversing circular polarization. Differential dispersion also leads to Faraday rotation, with both effects depending on the relative alignment of the polarization and magnetic field.

3.3. *Propagation of scalar vortex beams: Transfer of OAM*

When only the right-handed vortex beam $\Omega_R(0) = |\Omega|LG^R$ is present at the entrance ($z = 0$), the medium generates a left-handed component $\Omega_L(z)$ through parametric coupling governed by the coefficients a and c in Eqs. (30) and (32). The MB solutions in Eqs. (42) and (43) simplify to

$$\Omega_R(z) = a\Omega_R(0) = a|\Omega|A(r)e^{il\phi}, \tag{47}$$

$$\Omega_L(z) = c\Omega_R(0) = c|\Omega|A(r)e^{il\phi}. \tag{48}$$

where a and c depend on the propagation distance z and system parameters. The generated field $\Omega_L(z)$ is proportional to $\Omega_R(0)$, with the coupling strength dictated by c. Since both components share the same OAM charge l, the beam remains a scalar vortex (non-vectorized), despite the polarization conversion.

The polarization conversion and associated OAM transfer observed here originate from the magnetically induced closed-loop coherence in the tripod configuration. The transverse magnetic field establishes coherence between the ground-state Zeeman sublevels, enabling cross-coupling between left- and right-circular polarization components. As seen in Eqs. (25) and (26), even if only one polarization component is initially present, the cross terms drive the generation of the complementary component, which inherits the same OAM. This process requires no external seeding, as the internal coherence of the medium itself facilitates both polarization conversion and faithful OAM transfer.

Optics EXPRESS

The efficiency of $\Omega_L(z)$ generation and $\Omega_R(z)$ depletion is quantified by

$$\eta_1(z) = \frac{|\Omega_R(z)|^2}{|\Omega_R(0)|^2} = |a|^2 = \left|\frac{1}{2}\left[(e^{m_1 z} + e^{m_2 z}) + \frac{N_1 - N_3}{M}(e^{m_1 z} - e^{m_2 z})\right]\right|^2, \tag{49}$$

$$\eta_2(z) = \frac{|\Omega_L(z)|^2}{|\Omega_R(0)|^2} = |c|^2 = \left|\frac{N_2 \beta_T^2}{M}(e^{m_1 z} - e^{m_2 z})\right|^2, \tag{50}$$

which depend critically on the non-zero transverse coupling parameter β_T. This parameter closes the EIT system, making the system phase-sensitive and enabling energy exchange between polarization OAM components. Thus the OAM transfer and generation of the second vortex field Ω_L is only possible when both β_0 and θ are not zero.

Figures 7 and 8 illustrate the variation of ratios η_1 and η_2 as functions of magnetic field angle θ (in the range $\pi/30 \le \theta \le \pi/14$) and probe detuning Δ_p, respectively. In Fig. 7, we set $\Delta_p = 0$. For each value of θ, we calculate z_c using Eq. (37), and for this z_c, we determine η_1 and η_2 using Eqs. (49) and (50). From Fig. 7, we observe that η_1 and η_2 decrease as θ increases, indicating that the highest efficiency for generating a new vortex beam occurs at $\theta = \pi/30$. Larger angles reduce coherence, suppressing energy transfer.

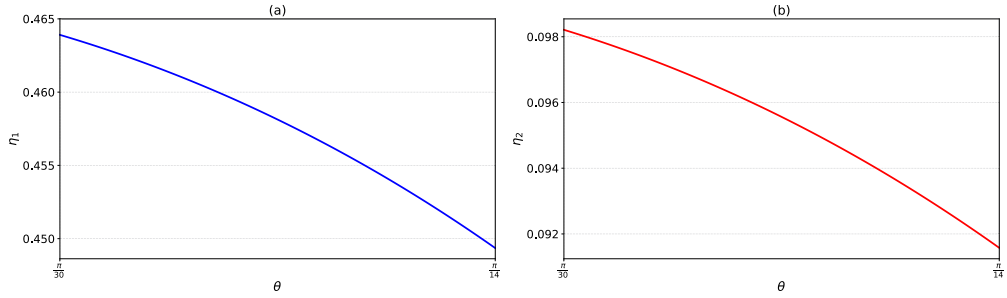

Fig. 7. Plots of efficiencies η_1 (a) and η_2 (b) as functions of magnetic field angle θ. The parameters used are the same as in Fig. 2.

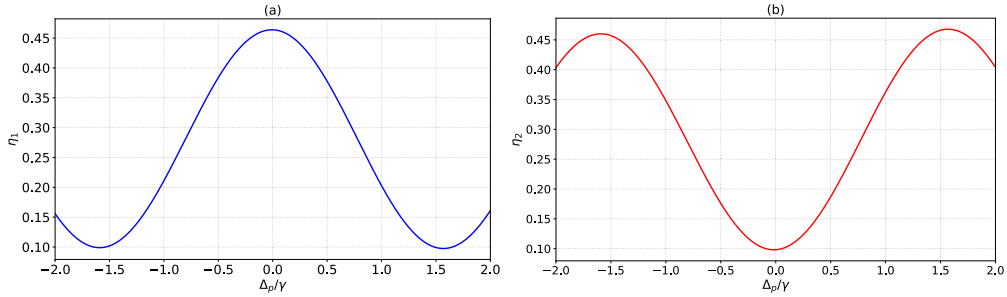

Fig. 8. Plots of efficiencies η_1 (a) and η_2 (b) as functions of probe detuning Δ_p. The parameters used are the same as in Fig. 3.

Next in Fig. 8, we fix $\theta = \pi/30$ and, for each value of Δ_p, we compute z_c using Eq. (37). Then, for the corresponding z_c, we evaluate η_1 and η_2 using Eqs. (49) and (50). In Fig. 8, the ratios η_1 and η_2 exhibit a periodic behavior with respect to Δ_p, implying that the conversion efficiency oscillates as a function of Δ_p. This oscillatory behavior may be linked to the exponential terms $e^{m_1 z}$ and $e^{m_2 z}$. If the real parts of m_1 and m_2 are small or if they contain imaginary components,

Optics EXPRESS

oscillations can arise. As the detuning Δ_p varies, m_1 and m_2 also change, directly affecting these exponential terms. Since m_1 and m_2 involve the square root M, which depends on Δ_p, M may become complex for certain detuning values. This could introduce an imaginary component in m_1 and m_2, leading to oscillations in $e^{m_1 z}$ and $e^{m_2 z}$, which in turn drive the periodic energy exchange between Ω_R and Ω_L, resulting in oscillations in the ratios η_1 and η_2.

Although our simulations focus on vector vortex beams with first-order OAM components ($l = \pm 1$), the general polarization evolution and OAM transfer mechanisms are expected to apply to higher-order vortex beams as well. Increasing $|l|$ will lead to more complex intensity and polarization patterns—such as a larger number of petals—but the fundamental dynamics governed by magnetic-field-induced coherence and OAM exchange remain qualitatively similar.

4. Concluding remarks

To summarize, we have explored the behavior of vortex beams (both polarization and phase vortices) as they propagate through a four-level tripod atom-light coupling system, where a transverse magnetic field plays a key role in mediating ground-state coherence. By solving the Maxwell-Bloch equations, we identified characteristic propagation distances where the linear response of the medium to the beam is maintained before the regime breaks down. For vector vortex beams consisting of left- and right-circularly polarized components with opposite angular momentum, the polarization structure and hence the atomic interaction is spatially varying. Before entering the medium, the beam exhibits a ring-shaped intensity profile with spatially varying polarization textures, consisting of polarization ellipses with radial, spiralling or azimuthal symmetry across the beam profile. However, as the beam propagates through the medium, we observed significant changes in both the intensity profile and polarization state. Specifically, the transverse intensity evolved from a ring to a petal-like shape, and the polarization state shifts between left-circular, linear, and right-circular forms. In particular, for non-resonant conditions, left-circular polarization can be completely transferred to right-circular polarization across the entire azimuthal plane. The observed spatially-dependent polarization dynamics can be attributed to the anisotropy of the atomic medium induced by a magnetic field. As such, it is determined by the interplay of magneto-optical effects, namely, circular birefringence and circular dichroism, leading to polarization rotation and ellipticity change, respectively. For phase vortex beams with uniform polarization (scalar vortex), we observe not a transverse spatial polarization modulation, but rather a longitudinal evolution of the polarization profile along the propagation direction. It is associated with a transfer of OAM between the beams of orthogonal circular polarizations due to a closed-loop configuration of the tripod scheme. This study enhances our understanding of the interactions between vortex beams and multi-level atomic systems, revealing novel possibilities for controlling OAM transfer. Finally, we note that our model is amenable to future experimental investigation. The tripod atom-light coupling scheme can be implemented as the $F = 1 \rightarrow F' = 0$ transition of the ^{87}Rb D_2 line. Our estimates of characteristic propagation distances are compatible with experiments, especially for near-resonant probe beams.

The current study focuses on the linear response regime, which enables analytical solutions to the Maxwell–Bloch equations and offers direct insight into the fundamental mechanisms governing polarization evolution and OAM transfer. This linear approximation is valid for weak probe fields and propagation distances shorter than a characteristic value z_c, beyond which absorption becomes significant and the linear model breaks down. However, at larger propagation distances $z > z_c$, we must go beyond the linear regime, which implies higher probe intensities or stronger atom–light interactions. In such conditions, nonlinear effects—such as optical Kerr nonlinearities— play a significant role. These effects could qualitatively alter the beam's intensity and polarization dynamics, as well as the efficiency of OAM transfer processes. A full treatment would require solving the nonlinear Maxwell–Bloch equations numerically, without the weak-field

Optics EXPRESS

approximation. While this lies beyond the scope of the present work, it is an important direction for future research.

Funding. Research Council of Lithuania (LMTLT) (agreement No. S-ITP-24-6); QuantERA II Programme, with funding received via the EU H2020 research and innovation programme (under Grant No. 101017733); Engineering and Physical Sciences Research Council (under Grant No. EP/Z000513/1 (V-MAG)); Anusandhan National Research Foundation, Government of India (under Grant No. CRG/2023/001318).

Acknowledgments. This project has received funding from the Research Council of Lithuania (LMTLT), agreement No. S-ITP-24-6. SF-A acknowledges support through the QuantERA II Programme, with funding received via the EU H2020 research and innovation programme under Grant No. 101017733 and associated support from EPSRC under Grant No. EP/Z000513/1 (V-MAG). T.N. D. gratefully acknowledges funding by the Department of Science and Technology, Anusandhan National Research Foundation, Government of India, under Grant No. CRG/2023/001318.

Disclosures. The authors declare no conflicts of interest.

Data availability. Data underlying the results presented in this paper are not publicly available at this time but may be obtained from the authors upon reasonable request.

References

1. L. Allen, M. W. Beijersbergen, R. J. C. Spreeuw, *et al.*, "Orbital angular momentum of light and the transformation of Laguerre-Gaussian laser modes," Phys. Rev. A **45**(11), 8185–8189 (1992).
2. M. Padgett and R. Bowman, "Tweezers with a twist," Nat. Photonics **5**(6), 343–348 (2011).
3. S. R. Park, L. Cattell, J. M. Nichols, *et al.*, "De-multiplexing vortex modes in optical communications using transport-based pattern recognition," Opt. Express **26**(4), 4004–4022 (2018).
4. R. Pugatch, M. Shuker, O. Firstenberg, *et al.*, "Topological stability of stored optical vortices," Phys. Rev. Lett. **98**(20), 203601 (2007).
5. M. Fleischhauer and M. D. Lukin, "Dark-state polaritons in electromagnetically induced transparency," Phys. Rev. Lett. **84**(22), 5094–5097 (2000).
6. M. Fleischhauer, A. Imamoglu, and J. P. Marangos, "Electromagnetically induced transparency: Optics in coherent media," Rev. Mod. Phys. **77**(2), 633–673 (2005).
7. M.-J. Lee, J. Ruseckas, C.-Y. Lee, *et al.*, "Experimental demonstration of spinor slow light," Nat. Commun. **5**(1), 5542 (2014).
8. J. D. Siverns, J. Hannegan, and Q. Quraishi, "Demonstration of slow light in rubidium vapor using single photons from a trapped ion," Sci. Adv. **5**(10), 1–5 (2019).
9. M. Sahrai, H. Tajalli, K. T. Kapale, *et al.*, "Tunable phase control for subluminal to superluminal light propagation," Phys. Rev. A **70**(2), 023813 (2004).
10. H. Wang, D. Goorskey, and M. Xiao, "Enhanced Kerr nonlinearity via atomic coherence in a three-level atomic system," Phys. Rev. Lett. **87**(7), 073601 (2001).
11. Y. Niu and S. Gong, "Enhancing Kerr nonlinearity via spontaneously generated coherence," Phys. Rev. A **73**(5), 053811 (2006).
12. H. R. Hamedi and G. Juzeliunas, "Phase-sensitive Kerr nonlinearity for closed-loop quantum systems," Phys. Rev. A **91**(5), 053823 (2015).
13. E. Paspalakis and P. L. Knight, "Electromagnetically induced transparency and controlled group velocity in a multilevel system," Phys. Rev. A **66**(1), 015802 (2002).
14. H. R. Hamedi, J. Ruseckas, and G. Juzeliunas, "Electromagnetically induced transparency and nonlinear pulse propagation in a combined tripod and Λ atom-light coupling scheme," J. Phys. B: Atom. Mol. Opt. Phys. **50**(18), 185401 (2017).
15. F. Bloch and I. I. Rabi, "Atoms in variable magnetic fields," Rev. Mod. Phys. **17**(2-3), 237–244 (1945).
16. L. Margalit, M. Rosenbluh, and A. D. Wilson-Gordon, "Degenerate two-level system in the presence of a transverse magnetic field," Phys. Rev. A **87**(3), 033808 (2013).
17. F. Renzoni, W. Maichen, L. Windholz, *et al.*, "Coherent population trapping with losses observed on the Hanle effect of the D_1 sodium line," Phys. Rev. A **55**(5), 3710–3718 (1997).
18. G. Walker, A. S. Arnold, and S. Franke-Arnold, "Trans-spectral orbital angular momentum transfer via four-wave mixing in Rb vapor," Phys. Rev. Lett. **108**(24), 243601 (2012).
19. D.-S. Ding, Z.-Y. Zhou, B.-S. Shi, *et al.*, "Linear up-conversion of orbital angular momentum," Opt. Lett. **37**(15), 3270–3272 (2012).
20. C. Yu and Z. Wang, "Engineering helical phase via four-wave mixing in the ultraslow propagation regime," Phys. Rev. A **103**(1), 013518 (2021).
21. Q.-F. Chen, B.-S. Shi, Y.-S. Zhang, *et al.*, "Entanglement of the orbital angular momentum states of the photon pairs generated in a hot atomic ensemble," Phys. Rev. A **78**(5), 053810 (2008).
22. J. Ruseckas, V. Kudriašov, I. A. Yu, *et al.*, "Transfer of orbital angular momentum of light using two-component slow light," Phys. Rev. A **87**(5), 053840 (2013).
23. H. R. Hamedi, J. Ruseckas, and G. Juzeliunas, "Exchange of optical vortices using an electromagnetically-induced-transparency–based four-wave-mixing setup," Phys. Rev. A **98**(1), 013840 (2018).

Optics EXPRESS

24. H. R. Hamedi, I. A. Yu, and E. Paspalakis, "Matched optical vortices of slow light using a tripod coherently prepared scheme," Phys. Rev. A **108**(5), 053719 (2023).
25. H. R. Hamedi, V. Kudriašov, J. Ruseckas, *et al.*, "Azimuthal modulation of electromagnetically induced transparency using structured light," Opt. Express **26**(22), 28249–28262 (2018).
26. S. Franke-Arnold, "Optical angular momentum and atoms," Phil. Trans. R. Soc. A **375**(2087), 20150435 (2017).
27. Q. Zhan, "Cylindrical vector beams: from mathematical concepts to applications," Adv. Opt. Photonics **1**(1), 1–57 (2009).
28. C. Rosales-Guzman, B. Ndagano, and A. Forbes, "A review of complex vector light fields and their applications," J. Opt. **20**(12), 123001 (2018).
29. A. M. Beckley, T. G. Brown, and M. A. Alonso, "Full Poincare beams," Opt. Express **18**(10), 10777–10785 (2010).
30. E. J. Galvez, S. Khadka, W. H. Schubert, *et al.*, "Poincare-beam patterns produced by nonseparable superpositions of Laguerre–Gauss and polarization modes of light," Appl. Opt. **51**(15), 2925–2934 (2012).
31. J. Wang, X. Yang, Y. Li, *et al.*, "Optically spatial information selection with hybridly polarized beam in atomic vapor," Photonics Res. **6**(5), 451–456 (2018).
32. L. Stern, A. Szapiro, E. Talker, *et al.*, "Controlling the interactions of space-variant polarization beams with rubidium vapor using external magnetic fields," Opt. Express **24**(5), 4834–4841 (2016).
33. A. M. Yao and M. J. Padgett, "Orbital angular momentum: origins, behavior and applications," Adv. Opt. Photonics **3**(2), 161–204 (2011).
34. N. Daloi and T. N. Dey, "Vector beam polarization rotation control using resonant magneto optics," Opt. Express **30**(12), 21894–21905 (2022).
35. N. Radwell, T. W. Clark, B. Piccirillo, *et al.*, "Spatially dependent electromagnetically induced transparency," Phys. Rev. Lett. **114**(12), 123603 (2015).
36. S. Sharma and T. N. Dey, "Phase-induced transparency-mediated structured-beam generation in a closed-loop tripod configuration," Phys. Rev. A **96**(3), 033811 (2017).
37. J. Wang, S. J. Svensson, T. W. Clark, *et al.*, "Measuring the optical concurrence of vector beams with an atomic-state interferometer," Phys. Rev. Lett. **132**(19), 193803 (2024).
38. P. Das and T. N. Dey, "Linear and nonlinear propagation of cylindrical vector beams through a nondegenerate four-level atomic system," Phys. Rev. A **110**(6), 063720 (2024).
39. F. Castellucci, T. W. Clark, A. Selyem, *et al.*, "Atomic compass: Detecting 3D magnetic field alignment with vector vortex light," Phys. Rev. Lett. **127**(23), 233202 (2021).
40. S. K. Hazra, P. K. Pathak, and T. N. Dey, "Arbitrary vector beam generation in semiconductor quantum dots," Phys. Rev. B **111**(3), 035419 (2025).
41. N. Daloi, P. Kumar, and T. N. Dey, "Guiding and polarization shaping of vector beams in anisotropic media," Phys. Rev. A **105**(6), 063714 (2022).
42. S. Ramakrishna, R. P. Schmidt, A. A. Peshkov, *et al.*, "Interaction of vector light beams with atoms exposed to a time-dependent magnetic field," Phys. Rev. A **110**(4), 043101 (2024).
43. R. Kumar, D. Manchaiah, and R. K. Easwaran, "Interaction of four level closed loop atomic systems in the presence of two vector beams," Phys. Scr. **98**(7), 075101 (2023).
44. D. Luo, H. Hu, C. Pan, *et al.*, "Nonlinear control of polarization rotation of hybrid-order vector vortex beams," J. Opt. **22**(11), 115612 (2020).
45. X. Zeng, Z. Li, X. Yang, *et al.*, "Spatial coherent manipulation of Bessel-like vector vortex beam in atomic vapor," New J. Phys. **26**(6), 063029 (2024).
46. Z. Li, S. Franke-Arnold, T. W. Clark, *et al.*, "Transfer and evolution of structured polarization in a double-V atomic system," Opt. Express **30**(11), 19812–19823 (2022).
47. V. D'Ambrosio, G. Carvacho, F. Graffitti, *et al.*, "Entangled vector vortex beams," Phys. Rev. A **94**(3), 030304 (2016).
48. K. Y. Bliokh, "Spatiotemporal vortex pulses: Angular momenta and spin-orbit interaction," Phys. Rev. Lett. **126**(24), 243601 (2021).
49. R. Kumar, D. Manchaiah, and R. K. Easwaran, "Theoretical study of a four-level EIT-type system in the presence of structured coupling light for microwave field detection," Appl. Opt. **61**(36), 10681–10687 (2022).
50. P. Azam, A. Griffin, S. Nazarenko, *et al.*, "Vortex creation, annihilation, and nonlinear dynamics in atomic vapors," Phys. Rev. A **105**(4), 043510 (2022).
51. T. Zhang, K.-K. Zhang, X. Deng, *et al.*, "Spatially dependent Raman gain by vortex beam in a four-level N-typed atomic system," Sci. Rep. **15**(1), 8650 (2025).
52. T. W. Clark, "Sculpting shadows. On the spatial structuring of fields and atoms: a tale of light and darkness, PhD thesis," University of Glasgow (2016).